Journal of Catalysis 395 (2021) 302–314

Contents lists available at ScienceDirect

Journal of Catalysis

journal homepage: www.elsevier.com/locate/jcat

Propene oligomerization on Beta zeolites: Development of a microkinetic model and experimental validation

Sergio Vernuccio [a,*], Elizabeth E. Bickel [b], Rajamani Gounder [b], Linda J. Broadbelt [c]

[a] Department of Chemical and Biological Engineering, University of Sheffield, Sheffield, United Kingdom
[b] Charles D. Davidson School of Chemical Engineering, Purdue University, West Lafayette IN, United States
[c] Department of Chemical and Biological Engineering, Northwestern University, Evanston IL, United States

ARTICLE INFO

Article history:
Received 4 September 2020
Revised 11 January 2021
Accepted 12 January 2021
Available online 21 January 2021

Keywords:
Oligomerization
Reaction network
Microkinetic model
Zeolite
Alkenes

ABSTRACT

The microkinetic modelling methodology that we developed previously to describe Brønsted acid-catalyzed propene oligomerization on medium-pore MFI zeolites has been extended successfully to large-pore Beta zeolites. The extension of the model was supported by the identification of the key descriptors that account for the different topologies and acid strengths of the zeolite frameworks (physisorption enthalpies, stabilization enthalpies, frequency factors). The model is validated with experimental conversion and selectivity data measured in a plug-flow reactor on a commercial Beta zeolite over a range of operating conditions. Analysis of net reaction rates allowed identifying the preferred pathways that increase oligomerization selectivity toward C_9 species with increasing propene pressure. The model was additionally used to investigate how the stabilization enthalpies of chemisorbed intermediates, an important catalyst descriptor, influenced the selectivity and surface coverage at *iso*-conversion. This analysis provides mechanistic insights into the propene oligomerization reaction network and its dependence on zeolite topology, and demonstrates how microkinetic models can describe catalyst behaviour and aid in catalyst and process optimization.

1. Introduction

The extraction of shale gas has increased rapidly in the US since the early 2000s, helping the US become the world's largest gas producer since 2009 [1,2]. The abundance and low cost of shale gas resources have spurred growing interest in routes to convert light hydrocarbon gases into liquid chemicals and transportation fuels [3,4]. Dehydrogenation of light alkanes to form alkenes and their subsequent oligomerization to heavier hydrocarbons is an attractive strategy to upgrade shale gas feedstocks into valuable chemicals and fuels. The use of Brønsted acidic zeolites to convert light alkenes into heavier oligomers was originally described in the Mobil olefin-to-gasoline and distillate (MOGD) process as a replacement for solid phosphoric acid catalysts [5–9]. In this reaction, Brønsted acid sites react with double bonds in alkenes to form carbocationic surface intermediates. These surface-bound species are reactants in the elementary steps of oligomerization reaction sequences and in side-reactions, including isomerization and cracking. These side-reactions add complexity to alkene conversion routes catalyzed by Brønsted acids that are typically described by large and highly interconnected reaction networks.

Kinetic models play an important role in reaction engineering for the development and optimization of chemical processes and design of novel catalytic materials. Several lumped kinetic models have been proposed in the literature to describe the oligomerization of alkenes [10–12]. The typical approach of these studies is to group several species based on their carbon number. While this strategy efficiently simplifies the structure of the models, it introduces several limitations to their broad applicability because of the multi-component nature of each group and the nature of certain assumptions used such as the assignment of one or more rate-determining steps. The microkinetic model methodology overcomes such limitations in typical pathways-level models by accounting for the rate of every elementary reaction involved in the network without assuming a rate-determining step. Microkinetic models are considered to have improved accuracy when applied to predict catalytic behaviour over wider ranges of operating conditions, but it comes at the expense of the increased computational time required for their solution.

Recently, we developed a microkinetic model for propene oligomerization on medium-pore, ten-membered ring (10-MR) MFI zeolite (i.e., ZSM-5) [13]. In this work, we extend this microki-

* Corresponding author.
E-mail address: s.vernuccio@sheffield.ac.uk (S. Vernuccio).

https://doi.org/10.1016/j.jcat.2021.01.018
0021-9517/

netic model methodology to describe the propene oligomerization process over the large-pore, 12-MR Beta zeolite. The reaction network that was originally built for ZSM-5 is used without any further adjustment. A set of zeolite framework specific catalyst descriptors were estimated with the aid of theoretical and experimental insights. The identification of these descriptors allows facile adaptation of the model to zeolites of different topology and acid strength. These properties influence the relative energies of reaction intermediates, transition states, and products, and thereby zeolite reactivity and selectivity.

The microkinetic model was validated by optimizing to product formation rates measured experimentally under different temperatures (483–503 K), pressures (122–319 kPa C_3H_6), catalyst loadings (0.01–0.05 g), and reactant flow rates (1.0–3.0 mol C_3H_6 (mol H^+ s)$^{-1}$). A microkinetic analysis elucidates the impact of these operating conditions on the dominant reaction pathways of the oligomerization network and thus was used to predict the effect of propene pressure on conversion and selectivity with the objective of providing insight into opportunities for process optimization. The effects of the stabilization enthalpies of surface-bound intermediates on the oligomerization kinetics are also investigated in detail. This predictive analysis can aid in efforts to design catalytic materials for process optimization and intensification.

2. Methods

2.1. Computational methods

2.1.1. Mechanism generation

The construction of the reaction network for Brønsted acid-based oligomerization chemistry is described in detail previously [13,14], and an abridged summary of the methodology used is provided herein. A set of physisorption/desorption steps describe the physical interaction of molecular species with acid sites. Physisorption steps involve the formation of a π-complex upon interaction of the double bond of an alkene with a Brønsted acid site [17]. The following protonation of the physisorbed alkene leads to the formation of a chemisorbed intermediate. Thus, the chemisorption enthalpy of an alkene is defined as:

$$\Delta H_{chem} = \Delta H_{phys} + \Delta H_{prot} \quad (1)$$

where ΔH is the enthalpy difference and the subscripts *chem*, *phys*, and *prot* indicate chemisorption, physisorption and protonation. The microkinetic model developed in this work treats chemisorbed species using a continuum approach and expresses the reaction rates in terms of surface coverages. The surface chemistry of the oligomerization process is described by eight surface reactions: protonation/deprotonation, oligomerization/β-scission, hydride shift, methyl shift, α-, and β-protonated cyclopropane (PCP) branching. It is worth noting that the chemisorbed intermediates could also undergo hydride transfer and cyclization reactions leading to the formation of alkanes, dienes, naphthenes and aromatics. However, among these species, only a negligible amount of alkanes was experimentally detected (<5 mol%). Thus, in order to limit the size of the network and the computational cost of the associated simulations, these additional reaction steps were not included in the model. Every reaction family is mathematically identified by a reaction operator in matrix form. This work employed the reaction generator NetGen [15,16] to automatically generate the kinetic network by applying the reaction operators to the connectivity matrices that represent the reactants and their progeny. Reaction rules were implemented to only consider and include molecular and chemisorbed species with carbon number lower than or equal to 9, because products of carbon number greater than 9 were not detected experimentally in significant quantities under the conditions studied. Due to the exponential increase of the number of generated species and reactions as a function of the termination criterion [14], an extension of the network to C_{12} species would result in a much larger network involving over 9 k species and over 60 k reaction steps. The increased computational cost that would be required for these simulations is not justified by the observed experimental results in the investigated range of low conversions. An extension of the model to predict higher conversion experimental results would require the inclusion of heavier species in the reaction network. The mechanism generation process resulted in a kinetic network composed of 269 gas-phase molecular species, 269 physisorbed molecular species, 371 chemisorbed intermediates and 4243 elementary reactions. The graphs of the molecules and the chemisorbed intermediates included in the network, divided based on carbon number and species type, are provided in Figs. S13–S26 of the Supporting Information.

We note that chemisorbed intermediates can have predominantly covalent (i.e., alkoxide) or ionic (i.e., carbenium ion) character dependent upon temperature, acid site geometry, and the degree of branching in the carbon backbone [17]. In this work, tertiary intermediates were treated as carbenium ions because their high degree of branching stabilizes positive charge more effectively than primary or secondary carbon centres. Primary and secondary chemisorbed intermediates were treated as alkoxides because they are more effectively stabilized via covalent bonding to zeolitic oxygen [18]. This treatment has significant implications for the frequency factors and the activation energies of the model because of the different enthalpies and entropies characteristic of covalent or ionic species. We note that all chemisorbed species are referred to using the symbol R^+.

2.1.2. Kinetic parameter determination

Table 1 lists the expressions of kinetic constants and reaction rates for the four categories of elementary steps included in the model: physisorption, 1st order surface reactions, 2nd order surface reactions, and desorption. The steps identified as 1st order surface reactions include deprotonation, β-scission and the isomerization steps (hydride shift, methyl shift, α-PCP-branching, and β-PCP-branching). The steps identified as 2nd order surface reactions include protonation and oligomerization. In Table 1, k is the reaction rate constant of an elementary step, and has units of measurement of 1/s for 1st order surface reactions and 1/(Pa s) for 2nd order surface reactions. r is the reaction rate, A is the frequency factor, E_a is the activation energy, R is the ideal gas constant, T is the temperature, ΔH_{phys} is the physisorption enthalpy, p_i is the partial pressure of species i in the gas phase, p_i^* is the pore pressure of species i, ϑ_i is the fractional coverage of surface species i or the fraction of empty sites.

Table 1
Expressions of kinetic constants (k) and reaction rates (r) for physisorption, surface reaction, and desorption steps.

	Kinetic Constant	Reaction Rate
Physisorption	$k = A$	$r = kp_i$
1st order Surface Reaction[a]	$k = A \cdot exp\left(-\frac{E_a}{RT}\right)$	$r = k\vartheta_i$
2nd order Surface Reaction[b]	$k = A \cdot exp\left(-\frac{E_a}{RT}\right)$	$r = kp_i^*\vartheta_j$
Desorption	$k = A \cdot exp\left(-\frac{\lvert\Delta H_{phys}\rvert}{RT}\right)$	$r = kp_i^*$

[a] The steps identified as 1st order surface reactions include deprotonation, β-scission, and the isomerization steps (hydride shift, methyl shift, α-PCP-branching and β-PCP-branching).
[b] The steps identified as 2nd order surface reactions include protonation and oligomerization.

The dependence of rate constants on temperature was described by the Arrhenius equation for each elementary step except for physisorption steps, which were considered to be non-activated processes. Therefore, for thermodynamic consistency, the activation energy of desorption of surface species i was equal to the physisorption enthalpy of the corresponding gas phase species.

The activation energy E_a of each elementary step was related to the reaction enthalpy according to the Evans – Polanyi relationship [19]:

$$E_a = E_0 + \alpha \Delta H_{rxn} \text{ for } \Delta H_{rxn} \leq 0 \quad (2)$$

$$E_a = E_0 + (1-\alpha)\Delta H_{rxn} \text{ for } \Delta H_{rxn} > 0 \quad (3)$$

where E_0 is an intrinsic energy barrier, ΔH_{rxn} is the reaction enthalpy, and α is the transfer coefficient of protonation, oligomerization, and forward isomerization that indicates the position of the transition state along the reaction coordinate. The general expectation is that more exothermic reactions are characterized by early transition states ($\alpha \to 0$) while more endothermic reactions are characterized by later transition states ($\alpha \to 1$). In case a negative activation energy was predicted using Eq. (2) or (3), E_a was set to 0 for exothermic reactions or to ΔH_{rxn} for endothermic reactions. In order to ensure thermodynamic consistency, the same value of the intrinsic energy barrier E_0 was selected for pairs of forward/reverse reaction families such that:

$$E_{a,forward} - E_{a,reverse} = \Delta H_{rxn} \quad (4)$$

To reduce the number of fitted parameters in the microkinetic model, we use the common assumption that elementary steps belonging to the same reaction family share the same kinetic parameters (A, E_0, α) and thus differ only by ΔH_{rxn}. The value of α was assigned based on the ranges of the reaction enthalpies of every family [20]. A value of $\alpha = 0.1$ was assigned to the oligomerization family that represents a class of highly exothermic reaction steps with $\Delta H_{rxn} > -34$ kcal/mol. A slightly higher value of $\alpha = 0.3$ was assigned to the moderately exothermic protonation family that includes reaction steps with $\Delta H_{rxn} > -22$ kcal/mol. Eq. (3) was used for their reverse steps, the endothermic β-scission and deprotonation. A sensitivity analysis depicted in Figs. S10 and S11 of the Supporting Information shows that the model predictions in terms of selectivity and conversion are markedly affected by the value of the transfer coefficient α of the coupled protonation/deprotonation and oligomerization/β-scission reaction families. Forward and reverse isomerization reactions were assigned a value of $\alpha = 0.5$, assuming a transition state located equidistant to reactants and products. The ratio of the intrinsic energy barrier for deprotonation of a tertiary carbenium ion and deprotonation of a secondary/primary alkoxide $\frac{E_{0,carbenium}}{E_{0,alkoxide}}$ was fixed to 0.3 to match the activation energy values reported for protonation of isobutene over acidic zeolites [32]. The sensitivity analysis depicted in Fig. S9 of the Supporting Information demonstrated that variations of this parameter within the interval [0,1] have a minor impact on the performance of the model. An analogous constraint was applied to protonation to respect the microscopic reversibility of the mechanism.

The reaction enthalpy ΔH_{rxn} of each elementary step was expressed as:

$$\Delta H_{rxn} = \Delta H_{rxn,g} - \sum_i \nu_i \cdot \Delta q\left(R_i^+\right) + \sum_j \nu_j \cdot \Delta H_{phys}\left(RH_j\right) \quad (5)$$

where $\Delta H_{rxn,g}$ is the enthalpy of reaction in the gas phase, R_i^+ and RH_j are respectively a generic chemisorbed intermediate and molecular species, ν indicates the positive (for products) or negative (for reactants) stoichiometric coefficient of each species in the elementary step, and Δq and ΔH_{phys} respectively represent the change in enthalpy due to stabilization of chemisorbed and physisorbed intermediates on the zeolite lattice. Note that ΔH_{phys} is a negative quantity. The reaction enthalpy in the gas phase $\Delta H_{rxn,g}$ was calculated based on Benson's group additivity method [21] using the group additivity values reported in a previous study [22]. Fig. 1 shows the theoretical physisorption enthalpies of n-alkanes [23] and 1-alkenes [24] as a function of the carbon number in ZSM-5 (MFI framework) and Beta (*BEA framework). The physisorption enthalpies of both alkanes and alkenes are systematically less negative by ~5–10 kJ mol^{-1} in Beta than in MFI because the smaller micropore size of MFI provides more effective van der Waals interactions between confined adsorbates and the zeolite lattice [25–27].

The physisorption enthalpies of the 269 neutral species included in the network were estimated using a group contribution method based on the type of each carbon atom. To determine the contribution of each single-bonded carbon atom to the physisorption enthalpy of a neutral species in Beta zeolites, we regressed the theoretical physisorption enthalpies of n-alkanes to carbon number (Fig. 1) to estimate a value of 0.53 kcal mol^{-1} for each sp^3 carbon atom. To determine the contribution of each sp^2 carbon atom, we subtracted the contribution of the sp^3 carbon atoms from the theoretical physisorption enthalpies of the normal alkenes reported in Fig. 1, to estimate that each sp^2 carbon atom provides an average contribution of 1.29 kcal mol^{-1} to the overall physisorption enthalpy of the molecule.

The physisorption enthalpy calculated using this group contribution method describes the physisorption of a gas-phase molecule on an empty site. However, it is reported in the literature that the physisorption enthalpy depends on the surface coverage of the zeolite and, when a site is occupied by an adsorbed molecule, a subsequent molecule has a weaker interaction with the pore of the zeolite. According to DFT studies, this reduced physisorption enthalpy can be estimated as 60% of the theoretical value calculated for an empty site [29,30]. Based on a sensitivity analysis over the ranges of operating conditions adopted in this work, surface-bound alkyls were verified to be present at saturation coverages. This is in agreement with the similar chemisorption free energies reported for propene in MFI and Beta [24] and the significantly higher propene pressures used in this work (122–319 kPa C_3H_6) at the same temperature (503 K) [28]. Sarazen *et al.* observed the disappearance of the Brønsted OH stretch by *in situ* IR measurements during propene oligomerization (503 K, 10 kPa C_3H_6) on

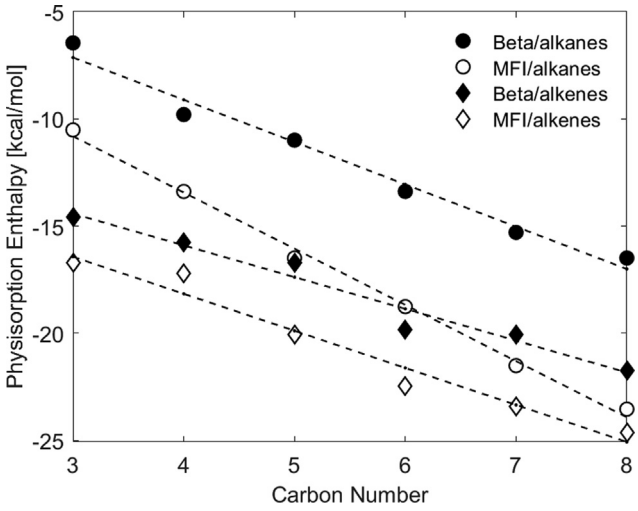

Fig. 1. Theoretical physisorption enthalpies of n-alkanes [23] and 1-alkenes [24] as a function of the carbon number in MFI and Beta.

H-form MFI zeolites, suggesting surface-bound alkyls were present at saturation coverages under these conditions [28]. For this reason, and based on the examples reported in the literature, the physisorption enthalpies of gas-phase molecules were estimated in this work as 60% of the theoretical value that is calculated by the group contribution method previously described.

The stabilization enthalpy of the chemisorbed intermediates is defined as the enthalpy difference between the gas-phase ionic species and the chemisorbed complex. This quantity can be calculated for every chemisorbed intermediate R_i^+ as:

$$\Delta q(R_i^+) = \Delta q(H^+) - \Delta H_{chem}(R_i) - PA(R_i) \quad (6)$$

where ΔH_{chem} is the chemisorption enthalpy of the gas-phase alkene R_i, PA is the proton affinity of the alkene, and $\Delta q(H^+)$ is the proton stability of Beta zeolite that is assumed to equal 272 kcal/mol [31]. The stabilization enthalpy of a chemisorbed species relative to that of a proton (relative stabilization enthalpy, $\Delta\Delta q(R_i^+)$) is defined as:

$$\Delta\Delta q(R_i^+) = \Delta H_{chem}(R_i) + \mathrm{PA}(R_i) \quad (7)$$

Table 2 displays the literature values for chemisorption enthalpies and proton affinities of C_2-C_9 alkenes and the relative stabilization enthalpies calculated according to Eq. (7). The chemisorption enthalpy of C_2-C_8 alkenes decreases linearly with carbon number because larger alkyls benefit more from van der Waals interactions with the confining zeolite pore. Extrapolation of this trend allows the estimation of the chemisorption enthalpy of 1-nonene. Fig. 2 shows a comparison between the calculated stabilization enthalpies of the secondary alkoxides of C_2-C_9 linear alkenes on Beta zeolite in this work and MFI zeolite from our prior work [13].

The chemisorption enthalpy of a given linear alkene on MFI is ~10 kJ mol^{-1} [24] more negative than on Beta, again a consequence of the smaller pore size of MFI compared to Beta [24]. The stability of covalently bound alkoxide adsorbates also depends on the lattice AlO_bSi angle in the chemisorbed complex, where O_b is the oxygen of the zeolite framework that is bonded to the carbon of the alkoxide [33]. This angle decreases much more significantly for adsorbates in MFI compared to Beta, suggesting greater lattice distortion is necessary for the formation of alkoxides in zeolites with smaller pores [24,34].

The relative stabilization enthalpy of the chemisorbed intermediates can be expressed as a function of the species type (i.e., primary, secondary, tertiary) and the carbon number according to [13]:

$$\Delta\Delta q(R^+) = \Delta H_{type} + a \cdot n_C + b \cdot n_C^2 \; with \; 3 \le n_C \le 9 \quad (8)$$

where n_C is the carbon number of the chemisorbed intermediate. Eq. (8) considers two different contributions for the stability of the chemisorbed intermediates: a large contribution depending on the ion type ΔH_{type}, and a much smaller contribution that is expressed as a function of the carbon number and accounts for the stabilization effect of the alkyl chain in the distribution of the positive charge along the carbon backbone.

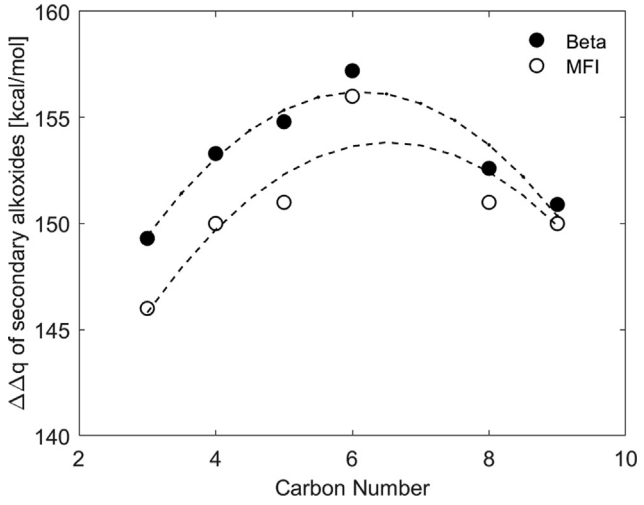

Fig. 2. Relative stabilization enthalpies for secondary alkoxides as a function of the carbon number in the range $3 \le n_C \le 9$ over Beta and MFI. The dashed lines are regression lines to fit the relative stabilization enthalpies that are computed in Table 2 using Eq. (8).

The dashed lines in Fig. 2 are best-fit regression of the relative stabilization enthalpies of secondary alkoxides (Table 2) to Eq. (8) to estimate parameters of $\Delta H_{sec} = 130.0 \frac{kcal}{mol}$, $a = 8.6$, and $b = -0.7$. The parabolic trend depicted in Fig. 2 for secondary species over Beta was scaled to match the stabilization enthalpies for the transformation of ethane to ethoxy (Table 2) by estimating $\Delta H_{prim} = 124.7 \frac{kcal}{mol}$. The parameter ΔH_{tert} was fixed to 158.0 kcal mol^{-1} by analogy with the trend reported in [13]. The higher values of the relative stabilization enthalpies on Beta with respect to the values previously calculated for MFI [13] are a consequence of lower chemisorption enthalpies for the larger pore Beta framework. We note that the parabolic trends in Fig. 2 apply specifically to alkoxides with carbon number $3 \le n_C \le 9$. For heavier hydrocarbons ($n_C > 9$), the stabilization enthalpy could possibly be expressed as a linear function of the carbon number by extrapolating the trends of chemisorption enthalpy and proton affinity of the alkenes reported in Table 2; however, we did not explore this aspect further because the maximum carbon number of the species considered in this study is $n_C = 9$.

2.2. Experimental methods

2.2.1. Characterization and pretreatment of beta zeolites

A Beta zeolite sample (Si/Al = 11) in NH_4-form was obtained from Zeolyst International. The number of Brønsted acid sites was quantified to be 9.0 × 10^{-4} mol H$^+$ g^{-1} by NH_3 temperature

Table 2
Chemisorption enthalpies and proton affinities of C_2 to C_9 alkenes and relative stabilization enthalpies of the corresponding alkoxide or carbenium ion on Beta zeolite.

species	π-complex → σ-complex	ΔH_{chem}[kcal/mol]	Ref	PA[kcal/mol]	Ref	$\Delta\Delta q(R^+)$[a] [kcal/mol]
primary	ethene → ethoxy	−28.5	[24]	168.4	[35]	140.0
secondary	propene → propoxy	−30.4	[24]	179.5	[36]	149.3
	1-butene → 1-butoxy	−31.6	[24]	184.7	[35]	153.3
	1-pentene → 1-pentoxy	−33.5	[24]	188.1	[35]	154.8
	1-hexene → 1-hexoxy	−35.4	[24]	192.4	[36]	157.2
	1-heptene → 1-heptoxy	−37.1	[24]	–	–	–
	1-octene → 1-octoxy	−38.5	[24]	191.0	[35]	152.6
	1-nonene → 1-nonoxy	−40.2	Estimated	191.0	Estimated	150.9

[a] Calculated using Eq. (7).

programmed desorption on the sample after aqueous-phase exchange with NH_4 cations at ambient temperature (1 M NH_4NO_3, Sigma Aldrich, 98%).

In a typical propene oligomerization experiment, a sample of NH_4-form zeolite was pelleted and sieved to retain particles of 180–250 μm diameter. The sieved zeolite sample (0.01–0.05 g) was diluted with SiO_2 (Sigma-Aldrich, high-purity grade, 180–250 μm) at zeolite/SiO_2 weight ratios of 0.05–0.15, and loaded into a stainless-steel reactor (9.5 mm i.d.) supported by quartz wool plugs and stainless-steel rods on both sides of the catalyst bed. The bed temperature was monitored with a K-type thermocouple placed in a concentric thermowell that extended through the axial center of the reactor such that the tip of the thermocouple was located at the center of the catalyst bed. The reactor was held within a furnace (Applied Test Systems, Series 3210) equipped with a temperature controller (Eurotherm 2408). An oxidative pretreatment (1.7×10^{-5} mol s^{-1} flowing air (air zero, THC < 1 ppm, Indiana Oxygen) and 5.1×10^{-5} mol s^{-1} flowing Ar (99.999% Indiana Oxygen)) was performed prior to oligomerization experiments. During pretreatment, the furnace temperature was increased to 823 K (1.5 K min^{-1}) for 5 h before cooling to reaction temperature (483–503 K).

2.2.2. Measurement of product formation rates for propene oligomerization

Reactant flows were composed of 75 mol% propene (99.9%, Matheson), 5 mol% methane (99.97%, Matheson), and 20 mol% Ar (99.999%, Indiana Oxygen). The pressure upstream of the catalyst bed was adjusted using a back-pressure regulator located downstream. Space velocity at a fixed propene partial pressure was adjusted (1.0–3.0 mol C_3H_6 (mol H^+ $s)^{-1}$) by changing the flow rate of propene (4.8×10^{-5}–1.1×10^{-4} mol s^{-1}) and the mass of catalyst in the packed bed (0.01–0.05 g). Fresh catalyst was used for each experiment. The reactor effluent was sent to a gas chromatograph (Agilent 7890A) equipped with a flame ionization detector (GS GasPro column, 0.320 mm i.d. × 60 m × 0 μm, Agilent) through lines heated to 390 K via resistive heating tape.

Products were quantified using methane as an internal standard every 28 min beginning at 10 min time-on-stream. The uncertainty in product molar flowrates was estimated based on the fluctuation of the reactant peak area relative to the internal standard peak area in GC analysis of the reactant stream performed when the reactor was bypassed. A representative product distribution is shown in Fig. S1 and Table S1 of the Supporting Information. Small amounts of alkanes (<5 mol%) were detected and lumped with alkenes of the corresponding carbon number for the estimation of selectivities. Product formation rates decreased as the catalyst deactivated with time-on-stream. Product molar flow rate transients were fit using an exponential decay model and extrapolated to zero time-on-stream to calculate selectivities and conversion prior to catalyst deactivation. Thus, all reported selectivities and conversions reflect product formation rates prior to catalyst deactivation and can therefore be interpreted on the basis of *ex-situ* H^+ site counts [37]. An example of transient formation rate data fitted to Eq. (S1) is shown for C_6 and C_9 products in Fig. 3.

The initial selectivity to primary products (i.e., C_6) decreased and the selectivity to secondary and higher rank products (i.e., C_9, β-scission products) increased with decreasing space velocity (Fig. S2, Supporting Information), consistent with previous reports and with predictions of the selectivity dependences of secondary and higher rank products on space velocity from a reaction pathway analysis [38,39].

Dimerization turnover rates were estimated by assuming all products originated from a dimerization step (Eq. (S3), Supporting Information) for the purpose of assessing bed-scale transport artifacts and in order to benchmark to previous literature reports.

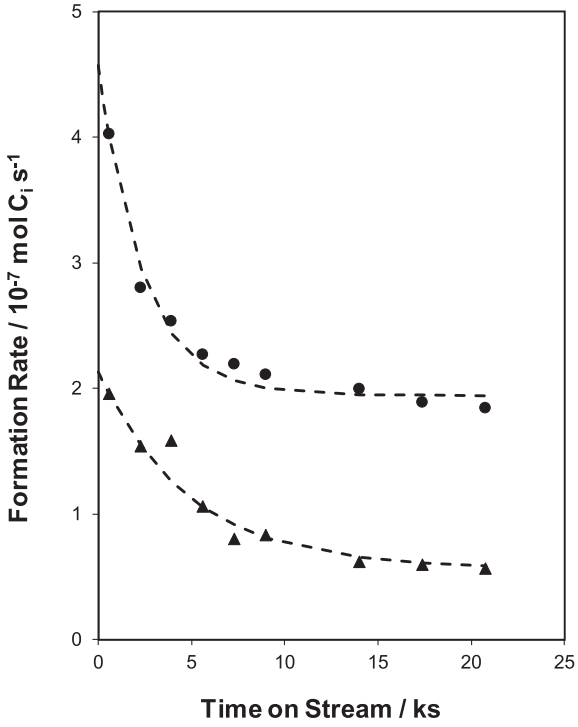

Fig. 3. Molar flow rates of C_6 products (circles) and C_9 products (triangles) produced from propene reactions (503 K, 169 kPa C_3H_6) on H-Beta (Si/Al = 11, Zeolyst). Dashed lines represent regression of the data to Eq. (S1), used to extrapolate formation rates of products of each carbon number (C_i) to zero time-on-stream to estimate initial rates.

Dimerization rates were extrapolated to zero time-on-stream using an exponential decay model to allow normalization of rates by *ex-situ* H^+ site counts (Fig. S3, Supporting Information) [37]. Initial dimerization turnover rates were independent of space velocity (Figs. S4 and S5a, Supporting Information) and extent of dilution with SiO_2 (Figs. S4 and S5b, Supporting Information), indicating that bed-scale temperature and propene concentration gradients were absent. Additionally, initial dimerization rates at 503 K plotted against propene partial pressure and fit with a first-order kinetic model (Fig. S6, Supporting Information) resulted in a first-order propene dimerization rate constant (1.0×10^{-4} mol (mol H^+ s kPa)$^{-1}$) that is within 2 × of a first-order propene dimerization rate constant at 503 K measured previously by Sarazen et al. on the same commercial H-Beta sample ($5.8\ 10^{-5}$ mol (mol H^+ s kPa)$^{-1}$) [28]. This factor of 2 × difference between our data and the previous data of Sarazen et al. on H-Beta zeolite is similar to the factor of 2 × difference in first-order rate constant (503 K) between our respective measurements for H-MFI (Fig. S7) [13,28]. Taken together, these observations indicate that the experimentally measured selectivities and conversion in this study are not corrupted by bed-scale heat and mass transfer artifacts and are quantitatively benchmarked to prior literature reports.

An apparent first-order dependence of propene dimerization rates on propene pressure would be consistent both with kinetic rate laws derived from proposed propene dimerization mechanisms [28] and with the presence of intracrystalline propene concentration gradients. An estimate of the Weisz-Prater criterion (Supporting Information S.3.) suggests that intracrystalline propene concentration gradients do not influence experimentally measured dimerization rates on the H-Beta sample used in this study, consistent with the conclusions of previous work at 503 K on the same sample [28]. These data cannot exclude the possibility of intracrystalline concentration gradients for higher molecular

weight products that participate in secondary and higher rank reactions (e.g., C_6), which have been proposed to influence selectivity to β-scission products [38]. For the purposes of this study, changes in rates of formation of all species in the reaction network are considered to be kinetic in origin.

3. Results

3.1. Model execution

The reaction rate forms listed in Table 1 were implemented into the design equation of a plug-flow reactor to reproduce the experimental results. The resultant set of differential and algebraic equations describing the change in partial pressure, pore pressure, and surface coverage was integrated via DDASAC [40], and frequency factors and intrinsic energy barriers tuning was performed using the gradient-based local optimizer GREG [41] by minimizing an objective function defined as:

$$\varphi = \sum_{i=1}^{n}\left[\sum_{k=4}^{9}\left(\frac{S_{C_{k,i}}^{exp} - S_{C_{k,i}}^{cal}}{\sqrt{0.1 S_{C_{k,i}}^{exp}}}\right)^2 + \left(\frac{X_i^{exp} - X_i^{cal}}{\sqrt{0.1 X_i^{exp}}}\right)^2\right] \quad (9)$$

where X is propene conversion defined as:

$$X = \frac{\sum_{k=4}^{9} k \cdot F_{C_k}}{3F_{C_3H_6}} \quad (10)$$

with F_{C_k} being the molar flow rate of the lumped species C_k and $F_{C_3H_6}$ is the molar flow rate of propene fed to the reactor. S_{C_k} is the selectivity to the species C_k defined as:

$$S_{C_k} = \frac{k \cdot F_{C_k}}{\sum_{k=4}^{9} k \cdot F_{C_k}} \quad (11)$$

In Eq. (9), $n = 6$ is the number of experimental runs involved in the estimation procedure. The subscripts exp and *cal* refer to experimental and calculated values. The values of the frequency factors (A) previously estimated for propene oligomerization on ZSM-5 [13] were initially assumed in this study. Optimization of these initial estimates (allowed to vary by one order of magnitude) was performed using five of the six experimental data sets measured at 503 K (Fig. 4) and one experimental data set at 483 K (Fig. 6), in order to account for the possible entropy differences engendered by the different zeolite frameworks. The sixth data set depicted in Fig. 4 (ratio of propene pressure and propene space velocity = 96.1 (kPa mol_{H+} s)/mol_{C3}) was used to assess the quality of the model prediction and as model validation. The selection of this data set for the validation procedure was randomized between the two sets with closest abscissa values, respectively 95.5 and 96.1 (kPa mol_{H+} s)/mol_{C3}. An additional constraint was imposed to maximize the alkoxide surface coverage of the zeolite during oligomerization in accordance with IR spectroscopy studies [28]. Each elementary step within a reaction family was considered to be characterized by the same entropy difference between reactants and transition states. This results in the same frequency factor for each elementary step of the same family.

The estimation converged when the relative change of each parameter was smaller than 10^{-5}. Overall, a total of 42 experimental points was used to estimate the 16 kinetic parameters listed in Table 3 together with their 95% confidence intervals. The frequency factors for deprotonation, oligomerization, β-scission, and isomerization reported in Table 3 are referenced to elementary steps involving alkoxides as reactants. The corresponding frequency factors for carbenium ions can be obtained by multiplying the values reported in Table 3 by 10^{-5} [32].

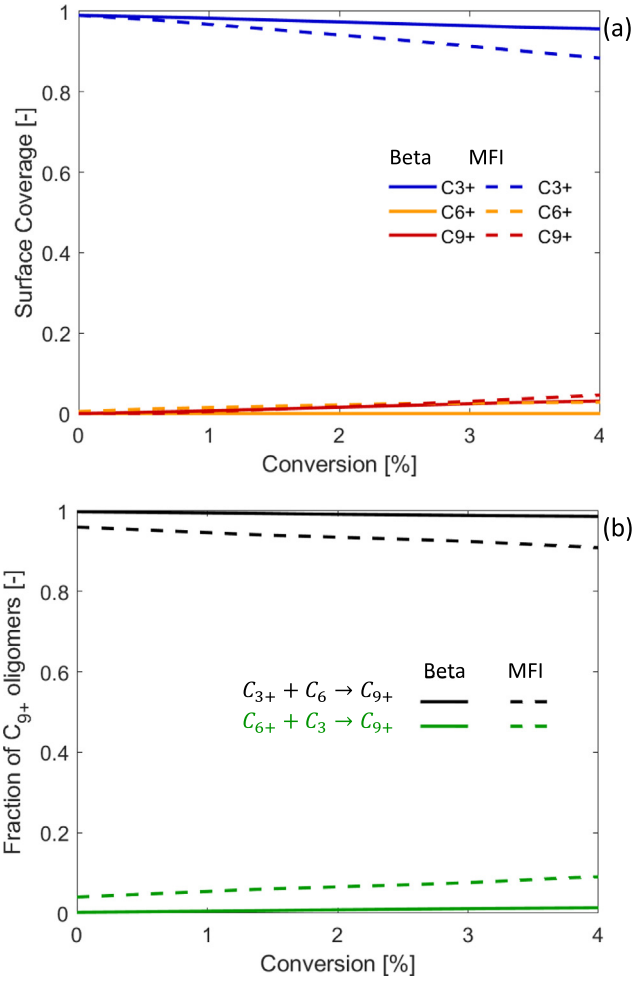

Fig. 5. (a) Surface coverage profiles at 503 K and feed propene pressure = 141 kPa of C_{3+}, C_{6+}, and C_{9+} species on Beta (solid lines) and MFI frameworks (dashed lines, [13]). Propene pressure is 75% of the total pressure. (b) Fraction of C_{9+} oligomers that originate from the addition of C_6 physisorbed molecules to propoxides (black) and from C_3 physisorbed molecules to C_6 chemisorbed intermediates (green) on Beta (solid line) and MFI (dashed line, [13]).

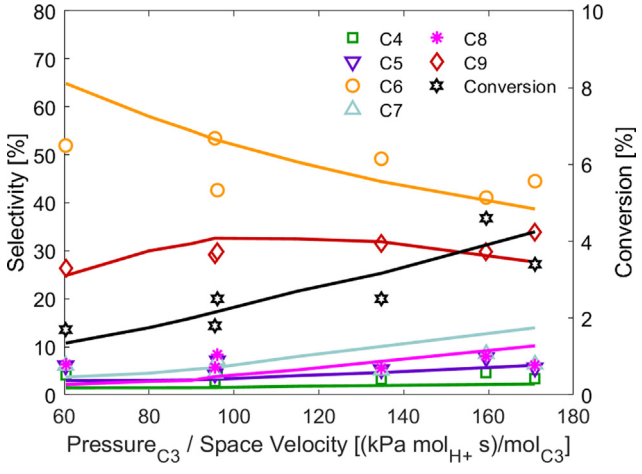

Fig. 4. Experimental (symbols) and calculated (lines) selectivity (left) and propene conversion (right) as a function of the ratio of propene pressure [kPa] and propene space velocity [$mol_{C3}(mol_{H+}\ s)^{-1}$] at 503 K. Propene pressure is 75% of the total pressure in the reactor. Experimental errors are 2% for selectivity and 0.1% for conversion.

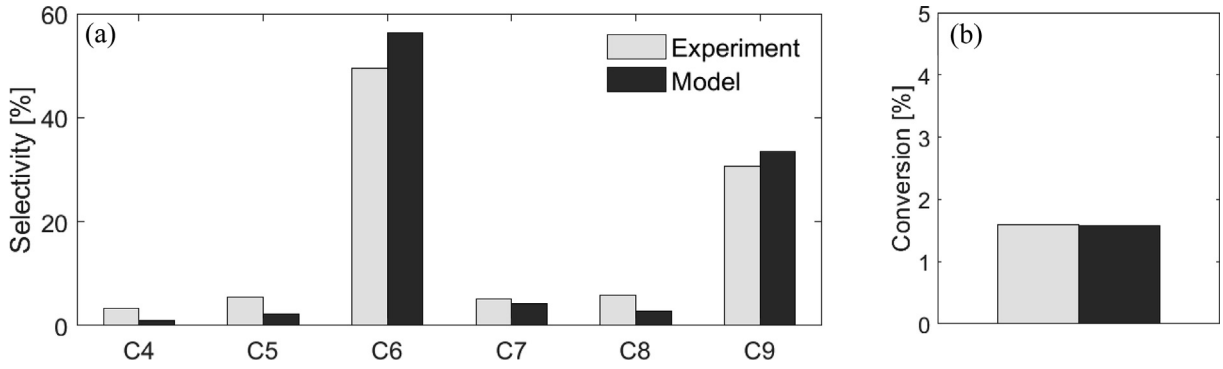

Fig. 6. Comparison of model results and experimentally-observed (a) selectivity and (b) conversion at 483 K. Propene pressure = 169 kPa; space velocity = 1.35 $mol_{C3}/(mol_{H+}$ s).

Table 3
Estimated Arrhenius frequency factors and Evans-Polanyi intrinsic energy barriers with 95% confidence intervals.

Reaction Family	A [1/(Pa s) or 1/s][c]	E_0 [kcal/mol]
Protonation[a]	$(9.2 \pm 1.0)\cdot10^{4}$	19.0 ± 0.6
Deprotonation[a,b]	$(1.0 \pm 0.5)\cdot10^{14}$	
Oligomerization[b]	$(1.5 \pm 0.1)\cdot10^{4}$	19.1 ± 0.2
β-Scission[b]	$(1.0 \pm 0.2)\cdot10^{14}$	
Hydride Shift[b]	$(6.0 \pm 0.5)\cdot10^{13}$	18.0 ± 3.0
Methyl Shift[b]	$(1.2 \pm 0.4)\cdot10^{13}$	10.1 ± 1.5
α-PCP-Branching[b]	$(1.0 \pm 0.2)\cdot10^{13}$	16.0 ± 2.0
β-PCP-Branching[b]	$(7.6 \pm 0.6)\cdot10^{13}$	8.0 ± 2.5
Physisorption	$(1.1 \pm 0.5)\cdot10^{1}$	–
Desorption	$(9.4 \pm 0.6)\cdot10^{7}$	–

[a] The intrinsic energy barrier E_0 for protonation and deprotonation is referred to elementary steps involving alkoxides.
[b] The frequency factors for deprotonation, oligomerization, β-scission, and isomerization are referred to elementary steps involving alkoxides as reactants.
[c] Frequency factors of first-order reactions and desorption have the units 1/s. Frequency factors of second-order reactions and physisorption have the units 1/(Pa s).

The frequency factors for oligomerization on Beta are approximately 10 × lower than the corresponding values estimated for MFI, consistent with apparent entropy losses when going from the physisorbed alkene to the transition state that become more negative as the zeolite pore size increases (MFI < MOR < FAU) as reported by Nguyen *et al.* [32]. All frequency factors were of order of magnitude 10^{13} for unimolecular isomerization steps, consistent with the assumption of no entropy change between reactants and isomerization transition states. The order of magnitude of 10^{-7} for the ratio A_{phys}/A_{des} is in good agreement with reported physisorption entropies of C_3-C_8 linear alkenes on Beta that range between −23.4 and −28.5 cal mol^{-1} K^{-1} [32].

No significant difference was observed in the intrinsic energy barriers E_0 that were estimated for Beta and MFI. The difference of E_0 of the reaction family pairs protonation/deprotonation and oligomerization/β-scission was estimated to be insignificant indicating that the difference in the activation energies of these reactions is mainly dictated by the differences in the reaction enthalpies rather than by the intrinsic nature of these elementary steps. In the same way, given the similarity of the reaction families, we would have expected the values of E_0 for hydride shift and methyl shift to be similar. However, forcing these values to be closer to each other resulted in larger discrepancies of the frequency factors, which have a more solid theoretical foundation, as they are related to the entropy of the species along the reaction coordinate according to the transition state theory.

The kinetic parameters for the isomerization kinetics listed in Table 3 were estimated using the Evans-Polanyi relations and regressions to experimental data at varying temperature to provide estimates of energy barriers. Detailed experimental data regarding the selectivity toward different isomers would be valuable information to validate the isomer distribution predicted by the microkinetic model and to reduce the relatively large uncertainties on the isomerization intrinsic energy barriers.

Fig. 4 shows the trend of experimental (symbols) and calculated (lines) conversions and selectivities as a function of the ratio of propene pressure and propene space velocity at 503 K. The quantity on the x-axis was chosen to combine the effects of space velocity and reactant pressure, in the form expected for a first-order rate law, on the selectivity and conversion. Increasing the propene pressure and decreasing the space velocity both result in increasing the ratio on the x-axis of Fig. 4, which leads to higher conversion for a fixed mass of catalyst. The model is able to capture the dependence of reactant conversion and the corresponding selectivity to different products (n_C = 4–9) on space velocity and pressure with an overall mean absolute error (MAE) of 32.3%. We note that this error largely arises from the higher than expected selectivity to β-scission products and lower than expected selectivity to C_6 products observed for the data set at 61 (kPa mol_{H+} s)/mol_{C3} (Fig. 4). The influence of intracrystalline mass transfer limitations on the egression of higher molecular weight oligomers from the zeolite may account for the deviations observed in this data set at high space velocity (i.e., low conversion) [38].

The microkinetic model can be used to estimate the detailed partial pressures and surface coverages of all isomers included in the network, even though the experimental data used to optimize the model provided selectivities based on lumped rates of formation of alkenes of different carbon number. Fig. 6 shows a comparison of calculated and experimental conversion and selectivity in which the model simulation was extended to a different temperature of 483 K.

The microkinetic models developed in the present paper (for Beta zeolite) and in our previous contribution (for MFI, [13]) were used to compare the performance of the zeolite frameworks in propene oligomerization. Fig. 5(a) shows the simulated surface coverage profiles of C_{3+}, C_{6+}, and C_{9+} at 503 K on Beta zeolites (solid lines – this study) and on MFI (dashed lines, [13]). In both cases, the fraction of empty sites is $O(10^{-3})$ (data not shown) indicating that the surface of the zeolite is fully covered with chemisorbed species. The MFI framework exhibits a higher surface coverage of C_{6+} and C_{9+} species than the Beta framework. Such trends might reflect the ability of MFI to better stabilize larger intermediates by van der Waals interactions, due to its smaller pore size than BEA, which would result in a higher coverage of C_{6+} and C_{9+} at equivalent pressure in the MFI framework. This analysis reveals an important finding regarding the origin of C_9 oligomers during propene

oligomerization on Beta and MFI. Fig. 5(b) shows the fraction of C_{9+} oligomers that originate from the addition of C_6 physisorbed molecules to propoxides (black) and from propene to C_6 chemisorbed intermediates (green) on Beta (continuous line) and MFI (dashed line). C_9 oligomers form predominantly through the addition of C_6 molecules to propoxides for both frameworks because of the dominant surface coverages of propoxides; however, Fig. 5(b) suggests that a much higher fraction of C_9 oligomers are formed by addition of propene to C_6 chemisorbed species on MFI than on Beta.

A comparison of the kinetic and thermodynamic parameters of the microkinetic models of propene oligomerization on Beta and MFI frameworks is reported in Table S2 of the Supporting Information.

3.2. Effect of the operating pressure

Fig. 7 depicts the simulated effect of propene pressure (75% of the total pressure) on the reaction selectivity at a constant propene conversion of 3.0%. Several simulations were conducted at 503 K by changing the operating pressure and adjusting the space velocity in the plug flow reactor to maintain constant conversion. Increasing the operating pressure results in a higher selectivity toward C_9 species at the expense of C_6 species. Furthermore, increasing the operating pressure has a negative effect on the occurrence of cracking side-reactions, as indicated by the lower selectivity toward C_4, C_5, C_7 and C_8 species.

During the simulations at different pressure, the model predicts that the acid sites are nearly fully covered with propoxides as depicted in Fig. 8, which shows the surface coverage at the point in the catalyst bed at which the conversion is 3.0% as a function of the feed propene partial pressure. The surface coverage of C_9 chemisorbed intermediates is significantly greater (by a factor 10^3) than that of C_6 intermediates and increases with operating pressure. The higher coverage of C_9 intermediates compared to that of C_6 is a result of the lower relative stabilization enthalpy ($\Delta\Delta q$) of C_9 chemisorbed intermediates or, in other words, of their more negative chemisorption enthalpies. This observation can be related to an analysis of the net rates that govern the oligomerization process. Fig. 9 shows a small section (44 pairs of forward/reverse reactions) of the oligomerization network including primary and secondary oligomerization steps of propene to C_6

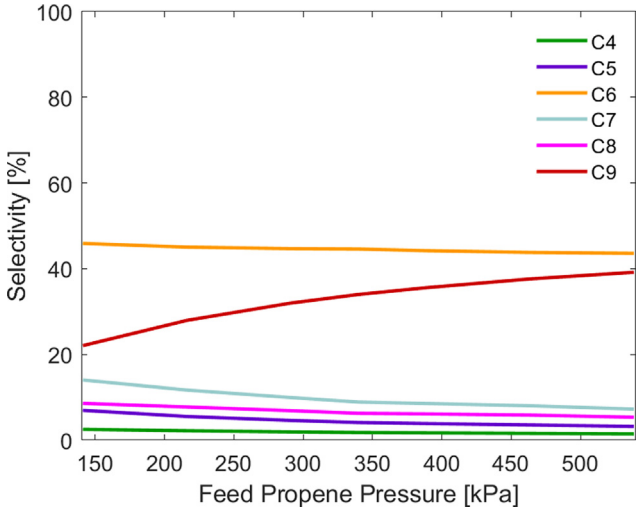

Fig. 7. Effect of the feed propene pressure on the selectivity of the oligomerization process at constant propene conversion of 3.0% and 503 K. Propene pressure is 75% of the total pressure.

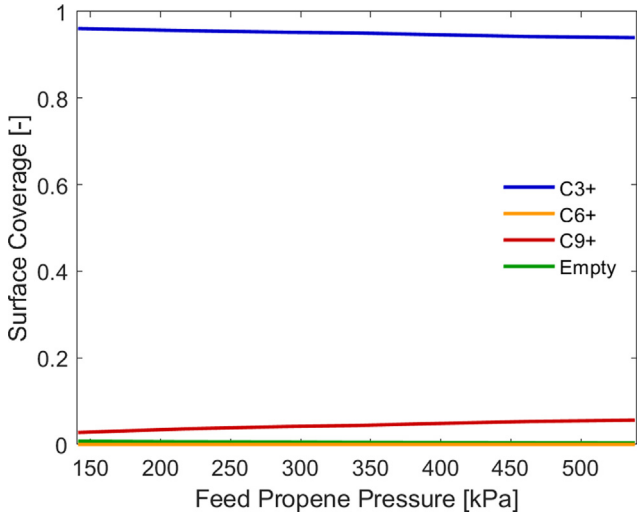

Fig. 8. Effect of the feed propene pressure on the surface coverage at constant propene conversion of 3.0% and 503 K. Propene pressure is 75% of the total pressure. The green line (empty) indicates the fraction of empty sites.

and C_9 species with the arrows pointing to species with a positive net rate of formation. The isomerization steps and the deprotonation of C_9 chemisorbed species are not shown for simplicity. The net rates are expressed in 1/s and are calculated at 503 K, a feed propene pressure of 141 kPa (black), 340 kPa (green) and 538 kPa (red), and a propene conversion of 3.0%. The values at different pressures are indicated in cases that the net rates at 141 and 538 kPa differ of a factor greater than 2×; otherwise only the value at 141 kPa is indicated. As indicated in Fig. 9, C_9 species can be generated by *i)* addition of propene to C_6 chemisorbed species or *ii)* addition of propoxides to C_6 physisorbed species. Under the investigated operating conditions and at a propene conversion of 3.0%, positive net rates of β-scission of C_9 species to C_6 chemisorbed intermediates (path *i*) were calculated, as depicted in Fig. 9. These reactions result in the formation of a C_6 alkoxide/ion and a molecule of propene from a C_9 species. This is consistent with the different surface coverages of C_9 and C_6 intermediates, as previously discussed in Fig. 8. The rates of these β-scission steps are not significantly affected by propene pressure. In the case of addition of propoxides to C_6 molecules (path *ii*), both positive and negative net rates of reactions were calculated for oligomerization to C_9 species in Fig. 9. Positive net rates of oligomerization (net rates towards heavy products), for example, justify the formation of 5-nonoxy, 5-methyl-4-octoxy, 3-isopropyl-2-hexoxy, 2,4-dimethyl-3-heptoxy, and 2-methyl-4-octoxy in Fig. 9. In these cases, increasing the propene pressure promotes the oligomerization of C_6 molecules as indicated in Fig. 9. In the case of positive net rates of β-scission, on the other hand, the kinetic constant of β-scission of C_9 species is greater than the kinetic constant of oligomerization to form such C_9 species. Oligomerization steps have lower barriers than β-scission steps; however, entropic contributions can lead to higher rate constants for the latter steps. The exemplary oligomerization pathway highlighted in the red box in Fig. 9 is reported in Fig. 10 showing the oligomerization pathway of propene to 2,3-dimethyl-1-heptoxy and to 5-nonoxy through dimerization of propene to 2-hexoxy. We deduced that, in the low conversion regime investigated here, the predominant secondary oligomerization products originate from C_9 chemisorbed species that are formed upon addition of C_6 molecules (i.e., primary oligomerization products) to propoxides.

The net rates of formation of 1-hexene (n_3), 2,3-dimethyl-1-heptoxy (n_4) and to 5-nonoxy (n_5) are reported in Fig. 11 as a func-

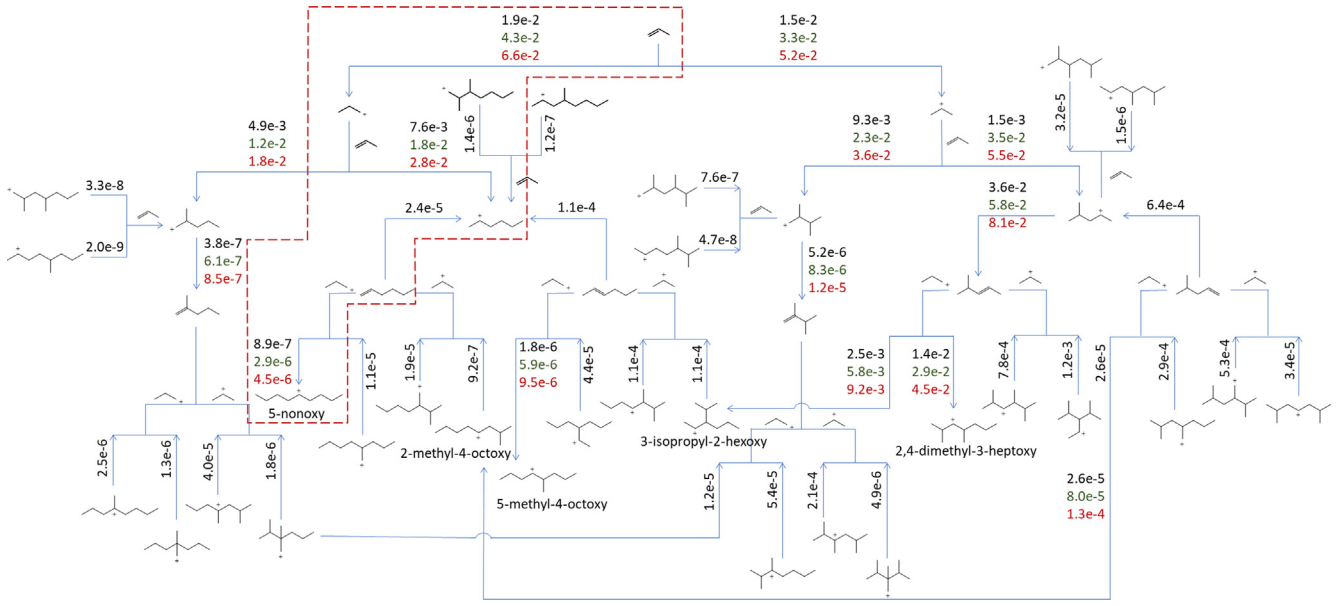

Fig. 9. Section of propene oligomerization pathway showing primary and secondary oligomerization steps to C_6 and C_9 species. The isomerization steps and the deprotonation of C_9 chemisorbed species are not shown for simplicity. Net rates of reaction are calculated at 503 K, at propene conversion of 3.0% and at a feed propene pressure of 141 kPa (black), 340 kPa (green), and 538 kPa (red). Values at different pressures are indicated in case that the net rates at 141 and 538 kPa differ of a factor greater than 2×; otherwise only the value at 141 kPa is indicated. The arrows point to the species with a positive net rate of formation.

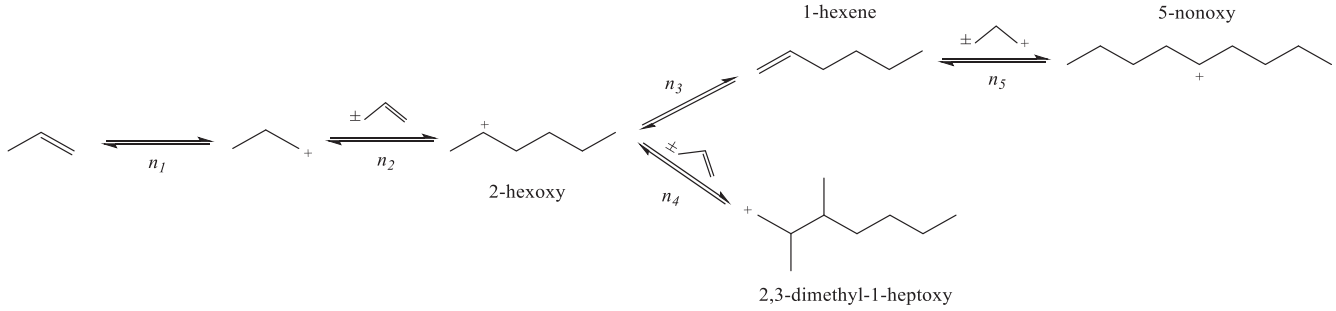

Fig. 10. Reaction pathway highlighted in the red box in Fig. 9 showing the exemplary oligomerization of propene to 2,3-dimethyl-1-heptoxy and to 5-nonoxy through dimerization to 2-hexoxy. Pathway n_3 + n_5 indicates deprotonation of 2-hexoxy and oligomerization of 1-hexene to a C_9 through addition of 1-propoxy. Pathway n_4 indicates oligomerization of 2-hexoxy to a C_9 through addition of propene.

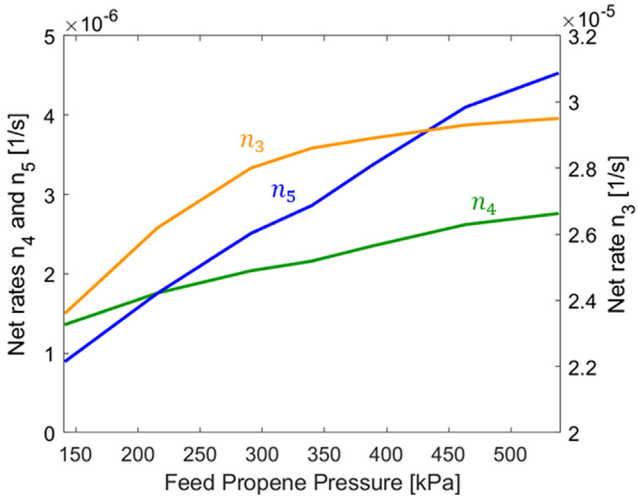

Fig. 11. Effect of the feed propene pressure on the net rates of formation/disappearance of 1-hexene (n_3), 2,3-dimethyl-1-heptoxy (n_4) and 5-nonoxy (n_5) with reference to the oligomerization pathway depicted in Fig. 10. Temperature = 503 K; Propene conversion = 3.0%.

tion of propene pressure. Increasing the operating pressure linearly increases the net rate of protonation of propene and the subsequent oligomerization to 2-hexoxy (Fig. S8, Supporting Information). The rate of protonation of 1-hexene to 2-hexoxy is 3 orders of magnitude greater than the reverse deprotonation rate in the range of investigated operating pressures. For this reason, the net rate of 1-hexene protonation/deprotonation n_3 can be approximated as:

$$n_3 \approx k_p p^*_{C_6} \vartheta_0 \tag{12}$$

where k_p is the kinetic constant of 1-hexene protonation, $p^*_{C_6}$ is the pore pressure of 1-hexene, and ϑ_0 is the fractional surface coverage of vacant sites. Increasing the operating pressure of the reactor increases the partial pressure of 1-hexene resulting in the trend of n_3 as a function of propene partial pressure depicted in Fig. 11.

2-Hexoxy can oligomerize to 2,3-dimethyl-1-heptoxy through addition of a physisorbed propene. However, the rate of β-scission of this chemisorbed C_9 species is 4 to 5 orders of magnitude greater than the reverse oligomerization rate in the range of investigated operating pressures. Therefore, the net rate of this forward/reverse elementary step can be approximated as:

$$n_4 \approx k_{\beta 4}\vartheta_{C_9^+} \quad (13)$$

where $k_{\beta 4}$ is the kinetic constant of 2,3-dimethyl-1-heptoxy β-scission to 2-hexoxy, and ϑ_i is the surface coverage of ionic species i. The trend of n_4 as a function of propene pressure in Fig. 11 is proportional to the surface coverage of the C_9 alkoxide and follows the increasing trend of C_9 chemisorbed intermediates reported in Fig. 8.

Another oligomerization pathway to obtain C_9 species is through addition of a propoxide to a C_6 physisorbed neutral species. As an example, the rate of oligomerization of 1-hexene to 5-nonoxy has the same order of magnitude of the corresponding rate of β-scission. The net rate of 1-hexene oligomerization/β-scission n_5 can be expressed as:

$$n_5 = k_o p^*_{C_6}\vartheta_{C_3^+} - k_{\beta 5}\vartheta_{C_9^+} \quad (14)$$

where k_o and $k_{\beta 5}$ are the kinetic constants of 1-hexene oligomerization and 5-nonoxy β-scission, respectively. Increasing the operating pressure results in an increase of both terms of Eq. (14), but the oligomerization rate is more affected by the pressure increase than the β-scission rate, resulting in the pressure dependence of n_5 depicted in Fig. 11. Higher pressures favor the oligomerization of C_6 physisorbed molecular species with propoxides over the reverse β-scission reaction, resulting in a more sustained production of C_9. It is worth noting that according to the net-rate analysis depicted in Fig. 10/11, 1-hexene is more rapidly consumed by protonation to 2-hexoxy and by oligomerization to 5-nonoxy than it is produced by the reverse deprotonation and β-scission steps. However, the overall oligomerization network includes many other reactions that generate 1-hexene and that are not included in Fig. 10 (e.g. β-scission of C_9 species, some of them illustrated in Fig. 9).

Overall, analysis of this exemplary oligomerization pathway provides mechanistic insight to rationalize the oligomerization selectivity profiles as a function of propene pressure. Higher pressures promote the oligomerization of C_6 to C_9 species through addition of physisorbed alkenes to propoxides, resulting in a more selective process toward C_9 species. This analysis confirms that, in the low conversion regime investigated in the present study, the oligomerization of propene on acidic zeolites is driven by the addition of C_6 physisorbed species to propoxides that cover the surface of the zeolite.

3.3. Effect of the stabilization enthalpy

The application of microkinetic models to catalyst design and discovery is related to the identification of a set of parameters that are often referred to as "catalyst descriptors" that account for the influence of critical material properties (e.g., bulk and atomic-scale structure and composition) of the catalyst on the kinetics of the process [42,43]. The microkinetic model-based search for new catalytic materials focuses on the optimization of these descriptors according to the desired optimal performance of the catalyst. In this work, the developed microkinetic model was used as a tool for preliminary catalyst optimization toward developing a more efficient oligomerization process. One of the main targets of the alkene oligomerization processes is the production of a product mixture that can be used as a gasoline blendstock, and a key metric in determining its economic value are research and motor octane numbers. In a recent contribution, some of the authors combined a microkinetic and octane number modelling approach to estimate the octane number of the effluent of an alkene oligomerization reactor. This study showed that, with specific reference to propene oligomerization over acidic zeolites, both research and motor octane numbers increase with increasing conversion because of the higher selectivity of the process to species with higher degree of branching [44]. For this reason, the selectivity of the process toward C_9 species was selected as the key parameter to identify optimized catalyst performance.

The translation of an optimal descriptor value into a physical property of the catalyst is a required next step in closing the catalyst design cycle [45]. It is worth noting that when translating the value of an optimized descriptor (e.g., the stabilization enthalpies of chemisorbed species) into a physical property of the catalyst, other catalyst descriptors (e.g. physisorption enthalpy, concentration of active sites) may also change and result in changes to the rates of various steps in the network. These final steps in closing the catalyst design cycle are beyond the scope of the present work.

The stabilization enthalpies of chemisorbed intermediates were selected as the primary catalyst descriptor of reference in this study because they depend directly on the acid strength of the zeolite framework. Furthermore, these parameters have a strong impact on the acid-catalysed oligomerization kinetics. As shown in this section, small changes in the values of the stabilization enthalpies result in a significant effect on propene conversion and process selectivity. For this analysis, the microkinetic model previously developed and experimentally validated was used to simulate the process selectivity of a plug flow reactor by varying the stabilization enthalpies at 503 K and at a feed propene pressure of 252 kPa. Several simulations were conducted by tuning the space velocity in order to obtain a constant conversion of 4.0% at the reactor outlet. In every simulation, the differences $\Delta\Delta H_t = \Delta H_{tert} - \Delta H_{sec}$ and $\Delta\Delta H_s = \Delta H_{sec} - \Delta H_{prim}$ were held constant.

Fig. 12 shows the catalyst surface coverage as a function of the species type-dependent stabilization enthalpies ΔH_{type} (only ΔH_{sec} is shown on the x-axis). The dash-dotted vertical line indicates the value of ΔH_{sec} for the zeolite framework (Beta) considered in this work. The green line (empty) indicates the fraction of empty sites. The gray line (β-scission) indicates the sum of the fractional surface coverages of C_{4+} and C_{5+}, chemisorbed species. The species type-dependent stabilization enthalpy is related to the relative stabilization enthalpy ($\Delta\Delta q$) through Eq. (8). Higher relative stabilization enthalpies of the chemisorbed intermediates result in a less exothermic chemisorption enthalpy of the corresponding molecular species (ΔH_{chem}) according to Eq. (7) and, as a consequence, in a

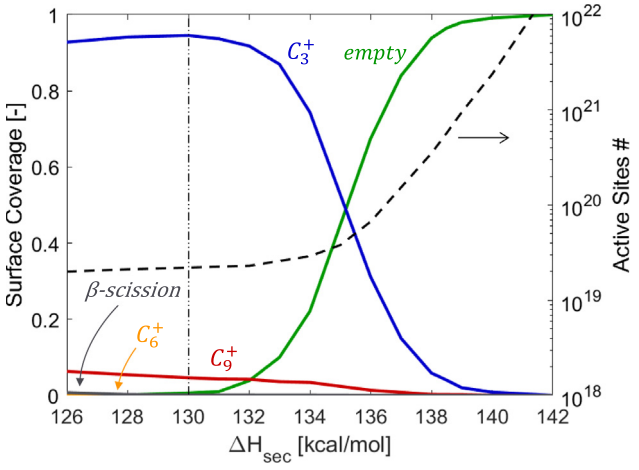

Fig. 12. Effect of the catalyst descriptor ΔH_{sec} on the surface coverage at constant feed propene pressure of 252 kPa, propene conversion of 4.0%, and 503 K. ΔH_{sec} is shown on the x-axis but ΔH_{prim} and ΔH_{tert} are changed accordingly to keep the differences $\Delta H_{tert} - \Delta H_{sec}$ and $\Delta H_{sec} - \Delta H_{prim}$ constant. The dash-dotted vertical line indicates the value of ΔH_{sec} for the zeolite framework (Beta) considered in this work. The green line (empty) indicates the fraction of empty sites. The gray line (β-scission) indicates the sum of the fractional surface coverages of C_{4+} and C_{5+} chemisorbed species. The dashed curved line (right axis) indicates the number of active sites considered in the simulations.

reduced total coverage of the acid sites. The fractional coverage of C_6 intermediates is always negligible compared to the corresponding coverage of C_9 species, which reflects the more favorable free energy of chemisorption of C_9 species. The coverage of propoxides is generally dominant due to the high partial pressure of propene in the reacting system.

The process selectivity is depicted in Fig. 13 as a function of the species type-dependent stabilization enthalpy ΔH_{type} (only ΔH_{sec} is shown on the x-axis). The gray line (β-scission) indicates the sum of the selectivity of the process toward C_4 and C_5 species. Increasing the stabilization enthalpy of the chemisorbed intermediates drives the selectivity of the process toward production of C_9 species at the expense of C_6 and β-scission species. The effect of ΔH_{type} on the net rates of formation of 1-hexene (n_3), 2,3-dimethyl-1-heptoxy (n_4) and 5-nonoxy (n_5) depicted in Fig. 10 is reported in Fig. S12 of the Supporting Information. At high relative stabilization enthalpies of the chemisorbed intermediates, these net rates tend to zero as a consequence of the lower coverage of the acid sites and the reduced activity of the catalyst.

The trend in Fig. 13 can be explained by the diagram in Fig. 14 that shows β-scission and deprotonation enthalpies of an exemplary C_9 secondary alkoxide (4-methyl-3-octoxy) and a tertiary C_9 carbenium ion (2,3-dimethyl-2-heptoxy ion) as a function of the stabilization enthalpies. ΔH_{sec} is indicated on the x-axis; as in the previous analysis, ΔH_{tert} and ΔH_{prim} were changed accordingly to keep the differences $\Delta\Delta H_t$ and $\Delta\Delta H_s$ constant. Negative enthalpies of reaction for deprotonation were set to 0.

The deprotonation of both these chemisorbed species leads to the formation of 4-methyl-2-octene, while the corresponding β-scission leads to the formation of 1-butoxy and a C_5 alkene. According to Eq. (4), the reaction enthalpy of β-scission is not affected by changes in stabilization enthalpy if the differences $\Delta\Delta H_t$ and $\Delta\Delta H_s$ remain constant. On the other hand, the reaction enthalpies of deprotonation linearly decrease with increasing the relative stabilization enthalpy (Eqs. (5)–(7)), indicating a weaker chemisorption of C_9 molecular species. Thus, designing a catalyst with a higher relative stabilization enthalpy $\Delta\Delta q$ (e.g., lower acid strength), would selectively disfavour tertiary ion chemisorption. Note that the relative stabilization enthalpy is defined by Eq. (7)

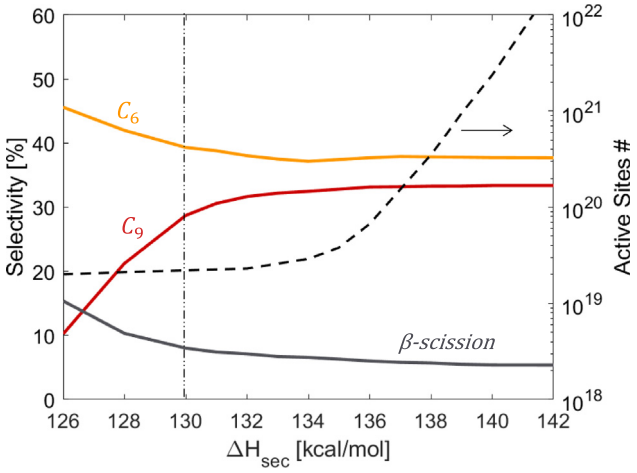

Fig. 13. Effect of the catalyst descriptor ΔH_{sec} on the process selectivity at constant feed propene pressure of 252 kPa, propene conversion of 4.0%, and 503 K. ΔH_{sec} is shown on the x-axis but ΔH_{prim} and ΔH_{tert} are changed accordingly to keep the differences $\Delta H_{tert} - \Delta H_{sec}$ and $\Delta H_{sec} - \Delta H_{prim}$ constant. The dash-dotted vertical line indicates the value of ΔH_{sec} for the zeolite framework (Beta) considered in this work. The gray line (β-scission) indicates the sum of the selectivities of the process toward C_4 and C_5 species. The dashed curved line (right axis) indicates the number of active sites considered in the simulations.

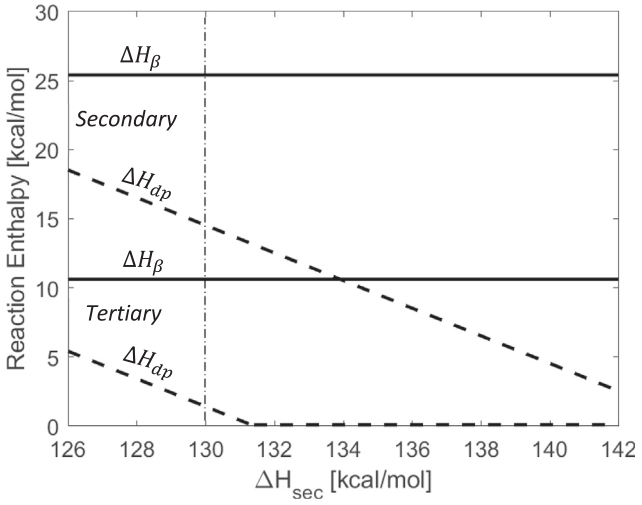

Fig. 14. Effect of the stabilization enthalpy of chemisorbed species on the reaction enthalpies of β-scission (ΔH_β, continuous line) and deprotonation (ΔH_{dp}, dashed line) of an exemplary secondary alkoxide (4-methyl-3-octoxy) and tertiary carbenium ion (2,3-dimethyl-2-heptoxy ion). Deprotonation of both these chemisorbed intermediates leads to the formation of 4-methyl-2-octene. β-Scission of these intermediates leads to the formation of 1-butoxy and a C_5 alkene. ΔH_{sec} is shown on the x-axis, but ΔH_{prim} and ΔH_{tert} are changed accordingly to keep the differences $\Delta H_{tert} - \Delta H_{sec}$ and $\Delta H_{sec} - \Delta H_{prim}$ constant. The dash-dotted vertical line indicates the value of ΔH_{sec} for the zeolite framework (Beta) considered in this work.

as a positive number. This would determine higher rates of formation of the molecular species that are directly derived from these reaction intermediates, resulting in an improvement of the selectivity of the process toward C_9 species. The acidity of the catalyst indicated by the range of $\Delta H_{sec} \in [126, 142]$ is sufficient to catalyse propene oligomerization and reach a conversion of 4.0%. However, further increases in the stabilization enthalpy would eventually significantly favour the deprotonation of primary species as well, resulting in a catalyst with acid strength insufficient to prefer any chemisorption and, therefore, any oligomerization chemistry.

It is worth noting that this analysis focuses on the optimization of the catalyst activity to obtain a higher selectivity of the process toward C_9 species, but does not consider aspects related to the reactor design. In order to maintain the conversion constant at 4.0% along the x-axis in Figs. 12 and 13, the space velocity in the reactor was drastically reduced. This was practically achieved by increasing the number of active sites in the fixed bed from 10^{19} to 10^{22} during the simulations, as indicated by the dashed curved lines in Figs. 12 and 13. Thus, for the sake of completeness, this solution should be associated with an economic analysis of the reactor design.

4. Conclusions

The microkinetic model developed in this work is able to capture the kinetic behaviour of propene oligomerization on acidic Beta zeolite at a variety of operating conditions. The physisorption and chemisorption enthalpies of the alkenes depend on van der Waals interactions, which become more negative with increasing carbon chain length and decreasing zeolite pore size. This work demonstrates how the fundamental nature of microkinetic analyses enables their broad applicability to different operating conditions and catalytic materials, such as varying zeolite frameworks. The extension of the model to additional frameworks is facilitated by identifying the key catalyst descriptors (physisorption enthalpies, stabilization enthalpies, frequency factors) that account for the effects of different catalyst material properties on the kinetics

of various elementary steps in the reaction network. An analysis of the effect of operating pressure shows that increasing propene pressure, at fixed conversion, results in a higher selectivity toward C_9 species. This occurs because the oligomerization step of C_6 to C_9 species is driven by the addition of chemisorbed propoxides to physisorbed C_6 alkenes, in the low conversion regime investigated in this study. A comparison of the simulated performance of MFI and Beta frameworks in the oligomerization of propene showed that on MFI a more significant quantity of C_9 oligomers is formed through addition of propene to C_6 chemisorbed species. This results from the ability of MFI to better stabilize larger intermediates through van der Waals interactions.

The last part of the work was dedicated to an analysis of the effect of the stabilization enthalpy towards the prospect of catalyst optimization. This study showed that the acid strength, which is directly related to the stabilization enthalpy of chemisorbed species, could be altered to selectively disfavour tertiary ion chemisorption resulting in an improvement of the selectivity of the process toward C_9 species.

Declaration of Competing Interest

The authors declare that they have no known competing financial interests or personal relationships that could have appeared to influence the work reported in this paper.

Acknowledgment

This paper is based upon work supported primarily by the National Science Foundation under Cooperative Agreement No. EEC-1647722. Any opinions, findings and conclusions or recommendations expressed in this material are those of the author(s) and do not necessarily reflect the views of the National Science Foundation. The authors acknowledge Lauren M. Lopez for the automated generation of the graphs of the species included in the reaction network and reported in the Supporting Information.

Appendix A. Supplementary material

Supplementary data to this article can be found online at https://doi.org/10.1016/j.jcat.2021.01.018.

References

[1] T. Bros, After the US Shale Gas Revolution, Technip, Paris, 2012.
[2] Y. Wang, W.E. Hefley, The Global Impact of Unconventional Shale Gas Development, Springer International Publishing, Cham, 2016.
[3] T. Ridha, Y. Li, E. Gençer, J.J. Siirola, J.T. Miller, F.H. Ribeiro, R. Agrawal, Valorization of shale gas condensate to liquid hydrocarbons through catalytic dehydrogenation and oligomerization, Processes 6 (2018) 139–160, https://doi.org/10.3390/pr6090139.
[4] J.A. Labinger, D.C. Leitch, J.E. Bercawl, M.A. Deimund, M.E. Davis, Upgrading light hydrocarbons: a tandem catalytic system for alkane/alkene coupling, Top. Catal. 58 (2015) 494–501, https://doi.org/10.1007/s11244-015-0380-2.
[5] W.E. Garwood, P.D. Caesar, J.A. Brennan, Light olefin processing. U.S. Patent 4 150 062, 1979.
[6] W.E. Garwood, W. Lee, Process for separating ethylene from light olefin mixtures while producing both gasoline and fuel oil. U.S. Patent 4 227 992, 1980.
[7] S.A. Tabak, Oligomerization of olefins, U.S. Patent 4 254 295, 1981.
[8] S.A. Tabak, B.S. Wright, H. Owen, Catalytic conversion of olefins to heavier hydrocarbons. U.S. Patent 4 504 693, 1985.
[9] R.J. Quann, L.A. Green, S.A. Tabak, F.J. Krambeck, Chemistry of olefin oligomerization over ZSM-5 catalyst, Ind. Eng. Chem. Res. 27 (1988) 565–570, https://doi.org/10.1021/ie00076a006.
[10] A.A. Mohammed, S.-E.K. Fateen, T.S. Ahmed, T.M. Moustafa, A kinetic model for ethylene oligomerization using zirconium/aluminum- and nickel/zinc-based catalyst systems in a batch reactor, Appl. Petrochem. Res. 4 (2014) 287–295, https://doi.org/10.1007/s13203-014-0047-0.
[11] P. Oliveira, P. Borges, R. Ramos Pinto, M.A.N.D.A. Lemos, F. Lemos, J.C. Vedrine, F. Ramoa Ribeiro, Light olefin transformation over ZSM-5 zeolites with different acid strengths – a kinetic model, Appl. Catal. A: Gen. 384 (2010) 177–185.
[12] P. Borges, R. Ramos Pinto, M.A.N.D.A. Lemos, F. Lemos, Vedrine, E.G. Derouane, F. Ramoa Ribeiro, Light olefin transformation over ZSM-5 zeolites. A kinetic model for olefin consumption, Appl. Catal. A 324 (2007) 20–29, https://doi.org/10.1016/j.apcata.2007.02.051.
[13] S. Vernuccio, E.E. Bickel, R. Gounder, L.J. Broadbelt, Microkinetic model of propylene oligomerization on Brønsted acidic zeolites at low conversion, ACS Catalysis 9 (2019) 8996–9008, https://doi.org/10.1021/acscatal.9b02066.
[14] S. Vernuccio, L.J. Broadbelt, Discerning complex reaction networks using automated generators, AIChE J. 65 (2019) 1–20, https://doi.org/10.1002/aic.16663.
[15] L.J. Broadbelt, S.M. Stark, M.T. Klein, Computer-generated pyrolysis modeling – on-the-fly generation of species, reactions, and rates, Ind. Eng. Chem. Res. 33 (4) (1994) 790–799, https://doi.org/10.1021/ie00028a003.
[16] M.T. Klein, G. Hou, R.J. Bertolacini, L.J. Broadbelt, A. Kumar, Molecular Modeling in Heavy Hydrocarbon Conversions, CRC Press, Taylor & Francis Group, Boca Raton, FL, 2006.
[17] P. Cnudde, K. De Wispelaere, J. Van der Mynsbrugge, M. Waroquier, V. Van Speybroeck, Effect of temperature and branching on the nature and stability of alkene cracking intermediates in H-ZSM-5, J. Catal. 345 (2017) 53–69, https://doi.org/10.1016/j.jcat.2016.11.010.
[18] M. Boronat, A. Corma, Are carbenium and carbonium ions reaction intermediates in zeolite-catalyzed reactions?, Appl Catal., A. 336 (1–2) (2008) 2–10, https://doi.org/10.1016/j.apcata.2007.09.050.
[19] M. Evans, M. Polanyi, Inertia and driving force of chemical reactions, Trans. Faraday Soc. 34 (1938) 11–29, https://doi.org/10.1039/TF9383400011.
[20] J.M. Martinis, G.F. Froment, Alkylation on solid acids. Part 2. Single-event kinetic modeling, Ind. Eng. Chem. Res. 45 (2006) 954–967, https://doi.org/10.1021/ie050910v.
[21] S.W. Benson, Thermochemical Kinetics: Methods for the Estimation of Thermochemical Data and Rate Parameters, John Wiley, Inc., New York, 1976.
[22] K. Bjorkman, C. Sung, E. Mondor, J.C. Cheng, D.-Y. Jan, L.J. Broadbelt, Group additivity determination for enthalpies of formation of carbenium ions, Ind. Eng. Chem. Res. 53 (2014) 19446–19452, https://doi.org/10.1021/ie503348z.
[23] B.A. De Moor, M.F. Reyniers, O.C. Gobin, J.A. Lercher, G.B. Marin, Adsorption of C2–C8 n-alkanes in zeolites, J. Phys. Chem. 115 (2011) 1204–1219, https://doi.org/10.1021/jp106536m.
[24] C.M. Nguyen, B.A. De Moor, M.F. Reyniers, G.B. Marin, Physisorption and chemisorption of linear alkenes in zeolites: a combined QM-pot(MP2//B3LYP:GULP)-statistical thermodynamics study, J. Phys. Chem. C 115 (2011) 23831–23847, https://doi.org/10.1021/jp2067606.
[25] F. Eder, M. Stockenhuber, J.A. Lercher, Brønsted acid site and pore controlled siting of alkane sorption in acidic molecular sieves, J. Phys. Chem. B 101 (1997) 5414–5419, https://doi.org/10.1021/jp9706487.
[26] F. Eder, J.A. Lercher, Alkane sorption in molecular sieves: the contribution of ordering, intermolecular interactions and sorption on Brondsted acid sites, Zeolites 18 (1) (1997) 75–81, https://doi.org/10.1016/S0144-2449(96)00127-3.
[27] C.E. Ramachandran, B.A. Williams, J.A. van Bokhoven, J.T. Miller, Observation of a compensation relation for *n*-hexane adsorption in zeolites with different structures: implications for catalytic activity, J. Catal. 233 (2005) 100–108, https://doi.org/10.1016/j.jcat.2005.04.017.
[28] M.L. Sarazen, E. Doskocil, E. Iglesia, Catalysis on solid acids: mechanism And catalyst descriptors in oligomerization reactions of light alkenes, J. Catal. 344 (2016) 553–569, https://doi.org/10.1016/j.jcat.2016.10.010.
[29] P.G. Moses, J.K. Norskov, Methanol to dimethyl ether over ZSM-22: a periodic density functional theory study, ACS Catal. 3 (2013) 735–745, https://doi.org/10.1021/cs300722w.
[30] Z. Fang, Y. Wang, D.A. Dixon, Computational study of ethanol conversion on Al_8O_{12} as a model for γ–Al_2O_3, J. Phys. Chem. 119 (2015) 23413–23421, https://doi.org/10.1021/acs.jpcc.5b05887.
[31] R.E. Patet, M. Koehle, R.F. Lobo, S. Caratzoulas, D.G. Vlachos, General acid-type catalysis in the dehydrative aromatization of furans to aromatics in H-[Al]-BEA, H-[Fe]-BEA, H-[Ga]-BEA, and H-[B]-BEA zeolites, J. Phys. Chem. C 121 (25) (2017) 13666–13679, https://doi.org/10.1021/acs.jpcc.7b02344.
[32] C.M. Nguyen, B.A. De Moor, M.-F. Reyniers, G.B. Marin, Isobutene protonation in H-FAU, H-MOR, H-ZSM-5, and H-ZSM-22, J. Phys. Chem. C 116 (34) (2012) 18236–18249, https://doi.org/10.1021/jp304081k.
[33] M. Boronat, P.M. Viruela, A. Corma, Reaction intermediates in acid catalysis by zeolites: prediction of the relative tendency to form alkoxides or carbocations as a function of hydrocarbon nature and active site structure, J. Am. Chem. Soc. 126 (10) (2004) 3300–3309, https://doi.org/10.1021/ja039432a.
[34] M.L. Sarazen, E. Iglesia, Stability of bound species during alkene reactions on solid acids, PNAS 114 (20) (2017) E3900–E3908, https://doi.org/10.1073/pnas.1619557114.
[35] B.A. De Moor, M.F. Reyniers, M. Sierka, J. Sauer, G.B. Marin, Physisorption and chemisorption of hydrocarbons in H-FAU using QM-Pot(MP2//B3LYP) calculations, J. Phys. Chem. C 112 (31) (2008) 11796–11812, https://doi.org/10.1021/jp711109m.
[36] E.P. Hunter, S.G. Lias, Evaluated gas phase basicities and proton affinities of molecules: an update, J. Phys. Chem. Ref. Data 27 (3) (1998) 413–656, https://doi.org/10.1063/1.556018.
[37] C. Costa, J.M. Lopes, F. Lemos, F. Ramôa Ribeiro, Activity–acidity relationship in zeolite Y: Part 1. Transformation of light olefins, J. Mole. Catal. A: Chem. 144 (1) (1999) 207–220, https://doi.org/10.1016/S1381-1169(98)00365-3.

[38] M.L. Sarazen, E. Doskocil, E. Iglesia, Effects of void environment and acid strength on alkene oligomerization selectivity, ACS Catal. 6 (10) (2016) 7059–7070, https://doi.org/10.1021/acscatal.6b02128.
[39] N.A. Bhore, M.T. Klein, K.B. Bischoff, The delplot technique: a new method for reaction pathway analysis, Ind. Eng. Chem. Res. 29 (2) (1990) 313–316, https://doi.org/10.1021/ie00098a025.
[40] W.E. Stewart, M. Caracotsios, J.P. Sorensen, Double precision differential-algebraic sensitive analysis code, Madison, WI, 1997, Version 1997, vol. 3.
[41] W.E. Stewart, M. Caracotsios, J.P. Sorensen, Generalized regression software (GREG), Madison, WI, 1997, Version 1997, vol. 3.
[42] J.W. Thybaut, J. Sun, L. Olivier, A.C. Van Veen, C. Mirodatos, G.B. Marin, Catalyst design based on microkinetic models: oxidative coupling of methane, Cat. Today 159 (2011) 29–36, https://doi.org/10.1016/j.cattod.2010.09.002.
[43] J.W. Thybaut, G.B. Marin, Single-Event MicroKinetics: Catalyst design for complex reaction networks, J. Catal. 308 (2013) 352–362, https://doi.org/10.1016/j.jcat.2013.08.013.
[44] H.S. Ganesh, D. Dean, S. Vernuccio, T.F. Edgar, M. Baldea, L.J. Broadbelt, M.A. Stadtherr, D.T. Allen, Product value modelling for a natural gas liquid to liquid transportation fuel process, Ind. Eng. Chem. Res. 59 (2020) 3109–3119, https://doi.org/10.1021/acs.iecr.9b06673.
[45] L. Pirro, P.S.F. Mendes, S. Paret, B.D. Vandegehuchte, G.B. Marin, J.W. Thybaut, Descriptor–property relationships in heterogeneous catalysis: exploiting synergies between statistics and fundamental kinetic modelling, Catal. Sci. Technol. 9 (2019) 3109–3125, https://doi.org/10.1039/C9CY00719A.